Additive Manufacturing 128 (2026) 105338

Contents lists available at ScienceDirect

Additive Manufacturing

journal homepage: www.elsevier.com/locate/addma

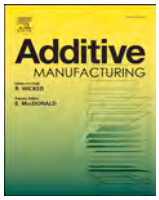

Transient interfacial melting promotes bonding in cold spray additive manufacturing of dissimilar metals

Arash Kardani [a], Matheus A. Tunes [b], Peter J. Uggowitzer [b], Hamid Assadi [c], Sara Bagherifard [a,*]

[a] Department of Mechanical Engineering, Politecnico di Milano, Milan, Italy
[b] Department Metallurgy, Chair of Nonferrous Metallurgy, Montanuniversität Leoben, Leoben, Austria
[c] Department of Engineering, Mechanical and Aerospace Engineering, Brunel University of London, Uxbridge, UK

ARTICLE INFO

Keywords:
Phase transition
High-velocity impact
Cold spray
Dissimilar metals
Molecular dynamics
Additive manufacturing

ABSTRACT

Understanding supersonic impact-induced bonding between dissimilar metals is important for advancing solid-state multi-material manufacturing. While established bonding mechanisms are typically based on plasticity-related indices and are defined for materials with similar properties, here we uncover a hidden dimension of thermo-dynamic mechanisms driving impact-induced bonding of mismatched metals. Atomic-scale simulations reveal transient melting initiating at the substrate surface upon impact and rapidly propagating across the interface. STEM-EDX analysis identifies an oxygen-rich interfacial layer (~17–20 nm), more than twice as thick as the native oxide, with SAED confirming new oxide formation. Band-shaped segregations within the Impact-Affected Zone (IAZ), ultrafine subgrains (~100 nm), and alloy-enriched precipitates adjacent to the IAZ are also observed. Together with the simulation results, these features are consistent with transient interfacial melting followed by rapid re-solidification. These findings highlight melting, rapid re-solidification, and the resulting microstructural transitions as significant contributors to metallurgical bonding in mismatched metallic systems, representing a thermodynamic pathway distinct from the widely accepted plasticity-based mechanisms. These insights advance the understanding of dissimilar-material joining and support the development of next-generation additive manufacturing technologies.

1. Introduction

Solid-state bonding technologies including Cold Spray (CS), Explosive Welding (EXW), Shock Welding (SW), Magnetic Pulse Welding (MPW), and Laser Impact Welding (LIW) are leveraged for joining and bonding materials through high-velocity impacts without noticiable melting [1–4]. Among the mentioned technologies, the CS process has attracted considerable attention from both academia and industry in recent years. Its appeal lies in its high deposition efficiency and build rate, together with its flexibility regarding component size and material selection. Furthermore, the process is well suited for a broad range of applications, including coating, repair, and additive manufacturing [5–7].

Particles with a diameter of 10–50 μm are accelerated to supersonic speeds in CS by passing through a convergent-divergent nozzle using a high-pressure pre-heated gas. The impact of these high kinetic energy solid particles onto a substrate's surface creates extreme thermodynamic conditions leading to both intense plastic deformation and localized heating at the particle-substrate interface, thereby leading to particle adhesion to the substrate [8]. The kinetic energy of the particles immediately prior to impact is the decisive factor governing the bonding strength and, consequently, the deposit quality. A key requirement for effective bonding is reaching a critical velocity, determined by the powder properties and process parameters. If the particles do not reach this critical velocity, they will rebound instead of bonding to the substrate [9,10]. Typically, critical velocities range from 500 to 1200 m/s, depending on powder's thermo-mechanical nature and morphology, along with other process parameters [10–12].

Bonding in CS occurs through a combination of metallurgical bonding and mechanical interlocking. The latter is primarily governed by particle morphology, substrate roughness, and the severe plastic deformation generated during impact [13]. This interlocking, however, can be mechanically weak and thus metallurgical bonding is required for the establishment of a robust interface. To accomplish metallurgical

* Corresponding author.
E-mail address: sara.bagherifard@polimi.it (S. Bagherifard).

https://doi.org/10.1016/j.addma.2026.105338
Received 10 April 2026; Received in revised form 5 August 2026; Accepted 8 August 2026
Available online 9 August 2026

bonding, the formation of a clean metallic interface, which enables atomic integration of the particle into the substrate, is required. Achieving such a clean contact area necessitates the impact energy to be sufficiently high to fracture native passive oxidic layers at the particle-substrate interface [14,15]. Native oxide disruption and fragmenting during impact promote exposure of clean metal surfaces [16,17]. Beyond surface properties, the internal structures of both the particle and substrate can also contribute to the development of strongly bonded interfaces. Secondary phases, precipitates, crystal defects, and micro-voids may hinder metallurgical bonding at the interface by increasing hardening of the substrate and the particle [18]. Assadi et al. [19] established that during the CS process, the intense localized heating generated by high-rate shear deformation at the particle–substrate interface is not effectively dissipated, primarily because the entire impact event occurs within an extremely short timescale—typically on the order of nano-seconds. Consequently, heat concentration at the interface induces localized thermal softening, overcoming strain hardening and leading to the formation of shear bands. This phenomenon, referred to as Adiabatic Shear Instability (ASI), enhances interfacial plasticity and promotes jetting. As a result, oxide layers, contaminants, and impurities are more effectively removed from the interface. ASI, however, has been conceived for the case where the counterparts are similar in properties; dissimilar bonding may involve different bonding pathways that merit dedicated investigations.

Formation of metallurgical bonding requires atomic incorporation across the interface, even when a clean metallic contact is present. However, a review of the current literature indicates that theories based on atomic diffusion, solid solution, or common molten phase solidification cannot fully account for bonding state observed in CS, due to the extremely short timescales and the negligible amount of melting involved [10,20]. Currently, there remains significant ambiguity regarding the exact atomic-scale mechanisms by which particle atoms integrate into the substrate to achieve metallurgical bonding, and the dominant mechanisms governing this phenomenon are not yet fully understood.

Based on our literature review, several authors have theorized the possibility of local melting in the impact zone. For instance, in an study depositing Zn onto stainless steel substrates, it was argued that potential melting would facilitate jet formation, thereby promoting particle-surface bonding [21]. In another study, dimples observed on the fracture surfaces of Ti and Ti6Al4V coatings deposited on a Ti6Al4V substrate were considered indicative of possible interfacial melting. The proposed melting mechanism was linked to the low thermal conductivity of the powder together with the occurrence of ASI. This interfacial melting, was mentioned as a side phenomenon potentially contributing to improved bonding [22]. Meanwhile, a few numerical studies have also suggested the occurrence of melting at the interface upon impact. In this context, Bae et al. [23] used Finite Element (FE) simulations to investigate the CS deposition of soft/hard material pairs, such as Ti-on-Al systems. The simulations indicated that the interfacial temperature could reach the melting point, potentially promoting interfacial bonding. Focusing on the upper band of the deposition window and thus erosion rather than bonding, Lucas et al. [24] recently developed Smoothed Particle Hydrodynamics (SPH) simulations to study the behavior of stainless steel 304 particles impacting a soft tin substrate. By comparing simulation data with SEM micrographs of impact-induced erosion craters, which showed splashing ejecta, it was concluded that high-velocity impacts leading to erosion caused significant melting on the substrate. The presence of this molten layer was attributed to adiabatic heating due to plastic dissipation.

While interfacial melting during CS has been suggested in several studies, the extent to which it contributes to particle–substrate bonding remains a subject of ongoing discussion. Further investigations are therefore needed to clarify its occurrence and significance. This research gap stems from the extremely thin thickness of this melted layer at the interface, which makes it challenging to confirm its significant contribution to bonding strength. Furthermore, due to the exceptionally brief timeframe of CS bonding, the interfacial molten phase is predicted not to undergo equilibrium solidification. However, our systematic study demonstrates that particle bonding extends beyond the direct interface, involving a broader region with significant microstructural changes named here as the Impact Affected Zone (IAZ). Beyond the particle–substrate interface, IAZ is affected by interfacial melting and heat generated by the high-velocity impact. These factors lead to significant microstructural modifications through localized melting and enhance bonding strength through the associated precipitation-hardening effect. Nevertheless, further attention is needed to clarify the roles of these aspects in CS bonding. Recrystallization and grain refinement are the most commonly reported phenomena in this zone. Previous studies have mainly attributed these features to sub-grain formation through dislocation rearrangement and grain boundary (GB) activities under high-strain-rate plastic deformation conditions [25–28]. In contrast, the potential roles of interfacial melting and thermal dissipation have received less attention.

In the present study, Scanning Transmission Electron Microscopy (STEM) characterization is combined with Molecular Dynamics (MD) simulations to investigate the fundamental atomic-scale mechanisms governing bonding between dissimilar metals during CS deposition. Fe particles are deposited onto an AA6082-T4 substrate as a representative hard/soft material pair. Particular emphasis is placed on the role of interfacial melting in bond formation. The choice of the Al-Fe system provided the ideal conditions for potential interfacial melting and enhanced recrystallization, due to Al's high thermal conductivity. Interestingly, the science of welding and joining these dissimilar metals (Al and Fe) is a historical metallurgical challenge of high technological relevance for many industries [29,30], and its underlying fundamentals are not yet fully understood [31]. Using MD simulations, we closely examined how the microstructure changes at the atomic level at the interface, aiming to clarify exactly how bonding occurs and what factors affect it during and after the particle's impact. Accordingly, the morphology, microstructure, and chemical composition of the interface were experimentally examined with STEM, providing experimental evidence that complements the atomistic simulations. Through the integration of advanced experimental characterization and atomic-scale modeling, this study improves the understanding of impact-induced bonding mechanisms. The resulting insights are relevant to multi-material manufacturing and solid-state joining applications.

2. Methods

2.1. Powder preparation and CS process parameters

Pure iron powder (99.64 wt%, Pometon S.p.A., IT) was sprayed onto an AA6082-T4 Al alloy substrate with a nominal composition was 0.97 wt% Si, 1.05 wt% Mg, 0.58 wt% Mn, 0.43 wt% Fe, and balance Al [32], using a high-pressure Impact Innovations 5/11 CS system (Impact Innovations, DE). The system utilized a converging-diverging SiC Out−1 nozzle with an expansion ratio of 5.6. Nitrogen served as process gas, set at 450°C and 50 bar pressure. A transverse velocity of 1600 mm/s was employed to facilitate the bonding of discrete particles to the substrate, rather than to achieve a continuous coating layer.

2.2. Characterization methods with electron microscopy

The specimen was placed within a FEI Apreo Scanning Electron Microscope operating at 20 keV and equipped with a Focused Ion Beam (FIB) system. An overview of the specimen as viewed by the backscattered-electrons detector (BSE) is shown in the supplemental information (See Fig. S1). After screening the sample within the SEM, we selected an area where Pt deposition was performed onto a Fe particle with diameter of around 13 μm. Sample preparation for S/TEM analysis was then performed following a procedure suggested by

Giannuzzi et al. [33,34]. We have used a standard Mo grid for the sample lift-out. In the final stages of ion polishing, the energy of the ion beam was reduced to mitigate damage and Ga implantation within the specimen.

After FIB, S/TEM was performed with a Thermo Fisher Talos F200X operating a Schottky field emission gun at 200 kV. For the characterization of the sample presented in this work, standard TEM techniques such as BFTEM and SAED were performed along with BF-, DF- and HAADF-STEM. Energy Dispersive X-ray spectroscopy was used to acquire elemental maps and quantification.

2.3. Molecular dynamics simulation details

The initial atomic configuration of the impact model, featuring a Fe particle and a pure Al substrate, is presented in Fig. S2. The Representative Volume Element (RVE) contains a total of 5008,517 atoms, with 4582,048 atoms forming the Al substrate, which measures 50 nm × 50 nm × 30 nm, exhibits a face-centered cubic (FCC) crystal structure, and has a lattice parameter of 4.04 Å. The remaining 426,469 atoms constitute the Fe particle, which has a diameter of 20 nm, demonstrates a body-centered cubic (BCC) crystal structure, and possesses a lattice parameter of 2.86 Å. As illustrated in Fig. S2, the substrate is divided into three distinct regions: a fixed layer that prevents rigid displacement of the substrate due to particle impact, a thermostat layer designed to stabilize the substrate temperature, and a Newtonian layer that is free to deform under impact, consistent with previous studies [25,35,36]. Oxide layers were not explicitly incorporated into the presented RVE. Their inclusion would substantially increase the complexity of the simulation system, the number of element involved, and the associated computational cost. Moreover, the primary objective of this study was to investigate the fundamental mechanisms governing metallurgical bonding at a clean metallic Fe–Al interface. Therefore, an ideal oxide-free interface was considered in the simulations in order to isolate and focus on the intrinsic interfacial bonding mechanisms.

The EAM–FS (Embedded Atom Model–Finnis–Sinclair) potential function was employed to describe the atomic interactions between Al-Al, Fe-Fe and Al-Fe atoms in the force and energy fields [37]. According to the previous studies, the standard form of the EAM potential function can successfully model the atomic diffusion of Al-Fe bicrystal samples during the mechanical loadings and annealing procedures [38,39]. However, it has been demonstrated that the introduced EAM–FS potential function provides more accurate outcomes regarding the interfacial features of the Al-Fe systems at a reduced computational expense [40]. The total potential energy in the EAM and FS formulations is expressed as the sum of an embedding-energy contribution and a pairwise interaction term [41]:

$$E_{total} = \sum_i F_{\tau_i}(P_i) + \frac{1}{2}\sum_i \sum_{j\neq i} \phi_{\tau_i\tau_j}(r_{ij}) \tag{1}$$

where $F_{\tau_i}(P_i)$ denotes the embedding energy associated with atom i, $\phi_{\tau_i\tau_j}(r_{ij})$represents the pair interaction potential between atoms $i$and j, and $r_{ij}$is the interatomic distance. The indices $\tau_i$and τ_j identify the atomic species of the interacting atoms.

The local electron density experienced by atom $i$is obtained by summing the density contributions from all neighboring atoms according to

$$P_i = \sum_{j\neq i} \rho_{\tau_i\tau_j}(r_{ij}) \tag{2}$$

where $\rho_{\tau_i\tau_j}(r_{ij})$represents the contribution of atom j to the local electron density at the position of atom i, and P_i denotes the resulting background electron density used in the embedding function.

The force acting on atom $i$is determined from the negative gradient of the total potential energy with respect to its position vector:

$$\mathbf{F}_i = -\nabla_{\mathbf{r}_i} E_{\text{tot}} \tag{3}$$

where $\mathbf{F}_i$is the force vector acting on atom i, and $\nabla_{\mathbf{r}_i}$denotes differentiation with respect to the coordinates of atom i. Substituting Eqs. (1) and (2) into Eq. (3) yields the explicit force expression:

$$\mathbf{F}_i = -\sum_{j\neq i}\left[\left(\frac{dF_{\tau_i}(P_i)}{dP}\frac{d\rho_{\tau_i\tau_j}(r_{ij})}{dr} + \frac{dF_{\tau_j}(P_j)}{dP}\frac{d\rho_{\tau_j\tau_i}(r_{ij})}{dr} + \frac{d\phi_{\tau_i\tau_j}(r_{ij})}{dr}\right)\frac{\mathbf{r}_i - \mathbf{r}_j}{r_{ij}}\right] \tag{4}$$

In Eq. (4), the first two terms inside the parentheses arise from the embedding-energy contribution and account for many-body interactions through the local electron density, while the last term corresponds to the direct pairwise interaction potential. The quantity $(\mathbf{r}_i - \mathbf{r}_j)/r_{ij}$is the unit vector directed from atom $j$toward atom i. This formulation enables EAM and FS potentials to accurately capture the many-body nature of metallic bonding, making them widely applicable in atomistic simulations of metals and alloys.

In this study, initial velocities were sampled by means of Maxwell–Boltzmann distribution at the specified temperature. To update position and velocity of atoms through solving equations of motions, Verlet integration algorithm was utilized. The value of 1fs was considered as the time-step to advance the system variables. The temporal evolution of the atomic system was integrated using the velocity-Verlet algorithm, which is widely employed in MD simulations because of its favorable energy conservation and numerical stability characteristics. In this scheme, the atomic positions are first updated according to [42]:

$$\mathbf{r}_i(t+\Delta t) = \mathbf{r}_i(t) + \mathbf{v}_i(t)\Delta t + \frac{1}{2}\mathbf{a}_i(t)\Delta t^2 \tag{5}$$

where $\mathbf{r}_i(t)$, $\mathbf{v}_i(t)$, and $\mathbf{a}_i(t)$denote the position, velocity, and acceleration vectors of atom $i$at time t, respectively, and $\Delta t$is the integration time step. Following the position update, the forces acting on the atoms are recalculated and the corresponding accelerations are obtained from Newton's second law:

$$\mathbf{a}_i(t+\Delta t) = \frac{\mathbf{F}_i(t+\Delta t)}{m_i} \tag{6}$$

where $\mathbf{F}_i(t+\Delta t)$is the force acting on atom $i$at the updated position and $m_i$is the atomic mass.

The atomic velocities are subsequently updated using the average acceleration over the time step:

$$\mathbf{v}_i\left(t+\Delta t\right) = \mathbf{v}_i(t) + \frac{1}{2}[\mathbf{a}_i(t) + \mathbf{a}_i(t+\Delta t)]\Delta t \tag{7}$$

This integration procedure ensures second-order accuracy in time and provides reliable trajectories for long MD simulations.

Before simulating the impact process, the sample was energy-minimized using the Conjugate Gradient (CG) algorithm to avoid any atomic overlap. The system was then equilibrated under the NPT ensemble (where the number of atoms and the pressure and temperature of the system remain constant) at 300 K and zero pressure for 10 ps under fully periodic boundary conditions [43,44].This preliminary equilibration step was performed to eliminate residual stresses and obtain a fully relaxed crystalline structure prior to impact. After NPT equilibration, the boundary condition along the z-axis was changed from periodic to non-periodic to create a free surface, while periodic boundary conditions were retained in the x- and y-directions. Subsequently, the particle and substrate were separately equilibrated under the NVT ensemble for 10 ps to relax their free surfaces prior to impact. During this stage, the temperature of the Al substrate was maintained at 300 K, whereas the Fe particle was heated to 673 K.

During impact simulations, the particle and Newtonian layer were evolved under the NVE ensemble (in which the number of atoms, system volume, and total energy remain constant), allowing deformation under

the stresses of collision [45]. Non-periodic boundary conditions were applied along the z-axis, perpendicular to the substrate [46], while periodic boundary conditions were maintained in the x- and y-directions. The particle impacted the substrate at velocities of 700–1200 m/s in 100 m/s increments, with a total simulation time of 30 ps. Fig. S3 presents a comparison between the final microstructure of the cold-sprayed specimen and the MD simulation. Fig. S3A shows a BSE-SEM image of the Fe particle embedded in the AA6082-T4 substrate at an estimated impact velocity of 597 m/s. The corresponding behavior of the particle in Fig. S3B confirms that our MD model and impact simulation reliably represent the behavior of current CS materials. Based on Computational Fluid Dynamics (CFD)-based KSS simulations and the model proposed by Assadi et al. [47], the predicted impact velocity of Fe particles with an average diameter of approximately 13 μm (corresponding to the dimension of the particle investigated in the TEM analysis) under the present CS conditions was estimated to be 597 m/s. However, due to the inherent dimensional limitations of MD simulations, a particle diameter of 20 nm was adopted in this study. Since the substantial difference in particle size results in significant changes in particle mass and impact energy, direct application of the experimentally predicted impact velocity is not appropriate. Therefore, an impact velocity of 1200 m/s was selected based on the range commonly employed in MD studies of particle impact and CS deposition ensuring bonding upon impact [43,48,49]. The Open Visualization Tool (OVITO) software package was implemented to visualize and analyze microstructural changes during the impact process [50]. To better distinguish the crystalline and disorder atoms, the PTM analysis tool was used. This modifier calculates local lattice orientation and elastic deformation gradient, providing accurate data even in the presence of significant heat fluctuations [51]. The grain segmentation modifier was employed to track the formation of new grains during the impact process [52]. Additionally, to identify the SFs, and GB regions, and disorder atoms, the Centrosymmetry Parameter (CSP) has been examined [53]. The CSP quantifies the deviation of an atom's local environment from perfect centrosymmetric. The results from this analysis tool are reported in Movie S1.

It should be noted that the MD simulations provide qualitative atomistic insight into the interfacial phenomena underlying the bonding process. Owing to the inherent differences in spatial and temporal scales, and the idealized oxide-free interface adopted in the simulations, the results should not be interpreted as a direct quantitative representation of the experimental CS process. Rather, they are intended to complement the experimental observations by providing mechanistic insight at the atomic scale. Establishing a rigorous quantitative connection between the simulations and experiments would require a comprehensive multiscale modeling framework, which is beyond the scope of the present study.

3. Results and discussion

3.1. Impact interface features observed by electron microscopy

The metallurgical effects of the Fe particle's high energy impact onto the AA6082-T4 alloy substrate are shown in Fig. 1. Fig. 1A presents the cross-section of the Fe particle attached to the AA6082-T4 substrate in the Dark-Field Scanning Transmission Electron Microscopy (DF-STEM) after the application of the Focused Ion Beam within the Scanning Electron Microscope (FIB-SEM) technique.

Three regions are noted along the interface and are enlarged with higher-magnification DF-STEM in Figs. 1B, 1C, and 1D. A slightly detached interface is observed at the center of the collision (Fig. 1C) whereas at the lateral regions, DF-STEM reveals the presence of a bonded interface between the Fe particle and the Al alloy substrate as shown in both Figs. 1B and 1D. The interface exhibits a distinctive "whitish" appearance. This characteristic feature is indicative of differences in both the crystal structure and local chemistry for DF-STEM. Under-focused Bright-Field Transmission Electron Microscopy (BF-TEM), Fig. 1E shows the regions where joining is established between the Fe-particle and the Al alloy substrate. The DF-STEM micrographs in Figs. 1B and 1D also reveal the presence of smaller grains (i.e., subgrains) in IAZ when compared with the unaffected areas of the substrate. IAZ appears to extend inner in the substrate up to a depth of ~500 nm. An analysis of the local chemistry within the IAZ is needed to further identify the metallurgical effects on the Al alloy substrate. We would like to note that the whitish contrast observed in the DF-STEM images should be interpreted with caution. Since DF-STEM contrast is primarily formed by diffracted electrons, the image intensity is mainly related to local crystallographic and microstructural variations. Nevertheless, compositional heterogeneities and local thickness variations may also contribute to the observed contrast. Therefore, the bright interfacial region cannot be solely attributed to a specific structural state based on DF-STEM observations alone. The corresponding SAED pattern exhibits Debye–Scherrer rings, indicating the presence of a nanocrystalline

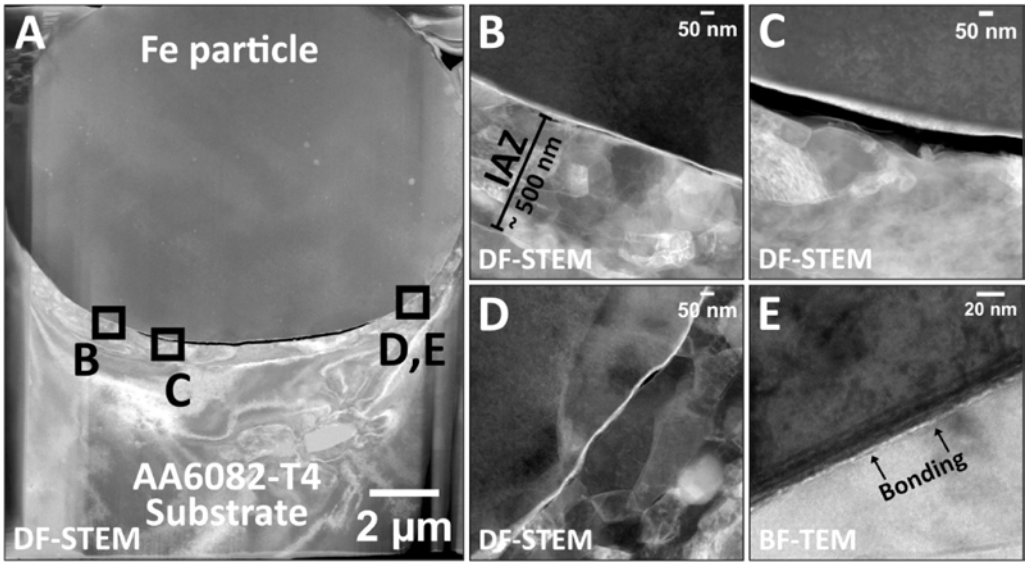

Fig. 1. Characterization of the impact interface showing in: A Fe particle after impact with the Al alloy (AA6082-T4) substrate. Higher-magnification micrographs taken along the interface reveal the formation of subgrains extending throughout the IAZ as shown in B, C, and D. Bonding is observed along the interface with under-focused BF-TEM as shown in E.

structure with randomly oriented grains, while EDX analysis confirms the existence of an oxygen-rich interfacial layer. These results together suggest that the observed contrast is associated with the combined structural and compositional characteristics of the interfacial region.

3.2. Analytical characterization of the IAZ using combined STEM and MD approaches

The local chemistry of the IAZ and its subgrain microstructure were further analyzed using Energy Dispersive X-ray (EDX) spectroscopy in STEM mode, as depicted in Fig. 2. The BF-STEM micrograph in Fig. 2A shows the analyzed area, whereas Figs. 2B and 2C exhibit the combined elemental maps of Al–O and Fe–O, respectively. A distinct O-rich layer is observed at the interface between the Fe particle and the AA6082-T4 substrate. The inset in Fig. 2A indicates that this O-rich layer has a thickness of around 17–20 nm, which is more than two times higher than the native oxides in 6xxx Al alloys [54].

The STEM-EDX analysis reveals significant metallurgical segregation in the IAZ. As shown in Fig. 2E, two non-equilibrium phases are formed. The elemental map of Si clearly indicates the presence of intra-granular Si-rich zones. Such pronounced segregation is clear evidence that a solid-liquid state was present in the IAZ, i.e. that the solidus temperature was exceeded and local melting took place. In view of the low Mg and Mn contents in AA6082 and for the sake of clearer visualization, the melting and segregation process is illustrated using the binary Al–Si phase diagram, as shown in Fig. 2D. The schematic diagram demonstrates that local Si enrichment caused by segregation shifts the alloy composition into the α + liquid region, thereby indicating the occurrence of local melting. It should be noted that the solvus temperature of Mg_2Si in AA6082 lies within the range of 500–550 °C [55]. This feature is not represented in the simplified binary Al–Si phase diagram. The section of the Al–Si binary phase diagram in Fig. 2D was constructed to illustrate the fractions of the liquid (red segment) and solid (blue segment) phases in the mushy zone formed in the IAZ. It is worth emphasizing that the nominal composition of the AA6082 alloy contains around 1 wt% of Si. Based on the rough assumption that the volume fraction of the Si-rich phase, i.e. the original liquid phase, is approximately 10% (Fig. 2E), the phase diagram indicates a Si enrichment of approximately 5 wt%. This aspect is further addressed in the evaluation of Fig. 6D. The observed Si-rich regions qualitatively indicate significant local Si enrichment resulting from segregation during transient melting. A quantitative estimation of the local Si concentration cannot be derived from the simplified binary phase diagram, which is intended only for schematic illustration of the melting and segregation process. The local

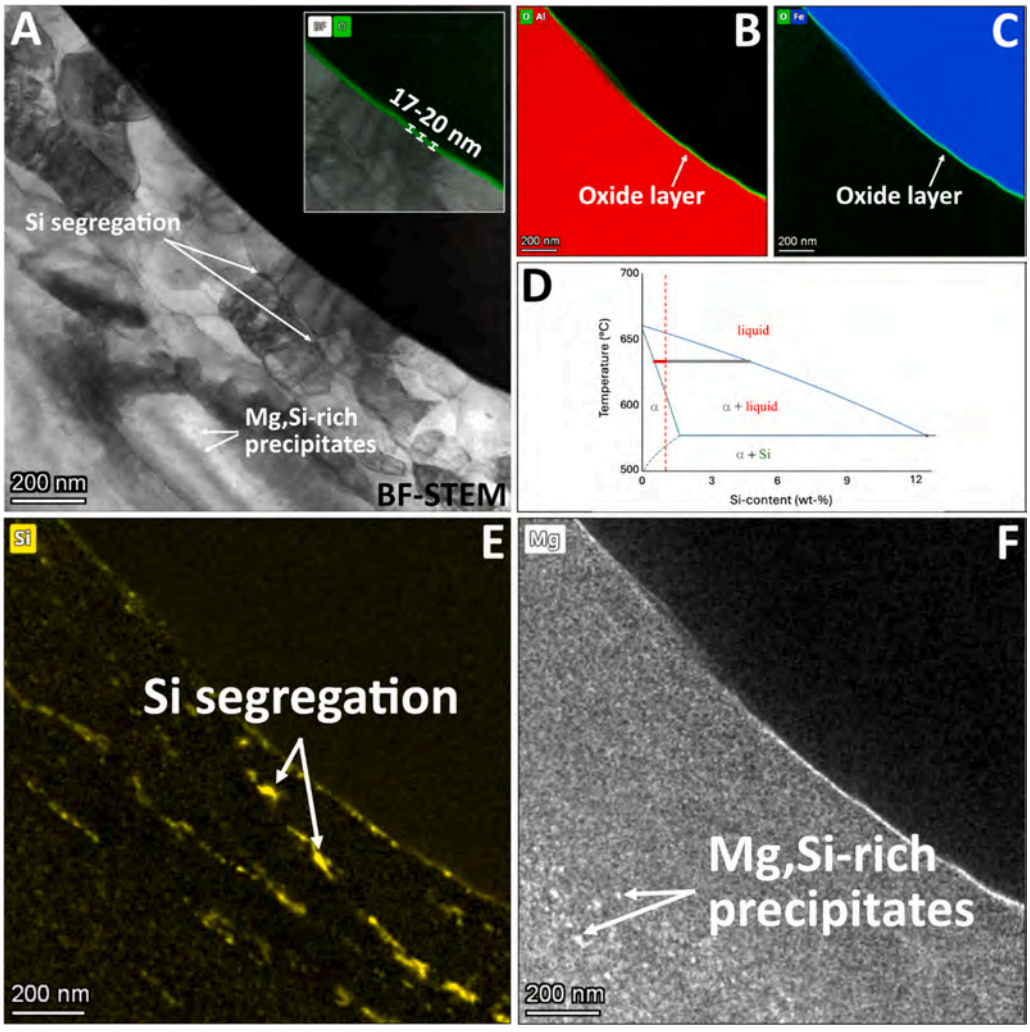

Fig. 2. Local chemistry analysis of the IAZ exhibited in the BF-STEM micrograph in A. B and C show combined Al-O and Fe-O elemental maps where a distinct O-rich layer is noted at the interface (measured to be ~17–20 nm thick as shown in the inset in A). The schematic of the Al-Si phase diagram shown in D exhibits the fractions of liquid (red segment) and solid (blue segment) phases as estimated from the elemental analysis. Both elemental maps of Si and Mg – E and F – taken along the IAZ show the presence of Si segregation in intra-granular positions and Mg,Si-rich precipitates at a deeper depth within the IAZ, but at trans-granular positions. Mg is also observed to enrich the interface with O as shown in F. Note: the elemental maps were normalized by at%.

chemical enrichment is discussed further in the evaluation of Fig. 6D.

Similarly, Mg, Si-rich precipitates are observed within the microstructure of the IAZ, but at a greater depth and in transgranular positions, as shown in Fig. 2F. It is worth emphasizing that Mg was also observed to segregate at the substrate interface with the Fe particle.

The formation of impact-induced Si-segregation (IIS) and impact-induced Mg-segregation (IIM) in the IAZ as well as for Mg and O at the interface between the Fe particle and the Al alloy substrate indicate that CS causes temporary and localized melting that encompasses the entire particle/substrate interfacial area and IAZ regions. We used MD simulations to analyze the nature of the interfacial melting development during different phases of impact. It should be noted that, due to the extremely fast timescale, localized effects, and temperature changes during the CS process, which happens at atomic scale, within nanoseconds and in partially liquid state, the actual sequence of CS events can only be represented in simulations and verified experimentally after the deposition process is complete.

Figs. 3 and 4 present the MD results in terms of atomic temperature distribution in both the Al substrate and Fe particle the during impact at a velocity of 1200 m/s, respectively. To provide a clearer interpretation of the thermal response, the temperature fields of the particle and substrate are presented separately. As shown in Fig. 3a-c, the atoms at the interface, which is only a few atomic layers thick, undergo a phase transition from crystalline to liquid state immediately as the particle impacts the substrate. Consequently, the temperature of the adjacent Al substrate reaches its melting temperature, leading to the formation of a thin molten interfacial layer.

The melting observed in this study is consistent with findings across both soft- and hard-material impact regimes. For example, the SPH simulations conducted by Lucas et al. [24] demonstrate definitive melting of a tin substrate during impact by a 304 stainless steel particle. As depicted in Fig. 3d, after a 10 ps time step, a significant portion of the interfacial atoms reached the *solidus* temperature of AA6082 (≈ 875 K). As the particle penetrates deeper into the substrate, a larger number of atoms in the substrate experience higher temperatures and form a mushy zone due to increased kinetic energy transfer promoted by both the impact and the intense subsequent plastic deformation. In contrast, the Fe particle remains well below its melting temperature (1811 K) throughout the impact event (See Fig. 4). Since the initial particle temperature is 673 K while the substrate temperature is 300 K, heat is continuously transferred from the particle to the colder substrate immediately after contact is established. As a result, the average particle temperature gradually decreases with increasing contact time and contact area. At later stages, the system undergoes thermal relaxation, and the interfacial temperature progressively decreases toward the ambient temperature, as illustrated in Fig. 3e–f. As the substrate dimensions in MD simulations may influence the simulation results due to finite-size effects, a substrate size sensitivity analysis was conducted by comparing two larger models, namely $80 \times 80 \times 60\ nm^3$ (~ 23.7 million atoms) and $70 \times 70 \times 50\ nm^3$ (~ 15.4 million atoms), with the original model of $50 \times 50 \times 30\ nm^3$ (~ 5.0 million atoms). The comparison of the atomic temperature distribution and deformation behavior demonstrated that the localized high-temperature region and interfacial deformation remained essentially unchanged, confirming that the substrate dimensions adopted in the present study are sufficient for accurately capturing the interfacial phenomena (See Fig. S4)

To further examine the occurrence of interfacial melting, radial distribution function (RDF) analysis was performed for different regions of the model. As shown in Fig. 5a, three representative regions, namely the particle, substrate, and interface, were selected at 30 ps for RDF calculations. The corresponding RDF profiles are presented in Fig. 5b–d. The RDFs of the particle and substrate regions (Figs. 5b and 5c) exhibit a

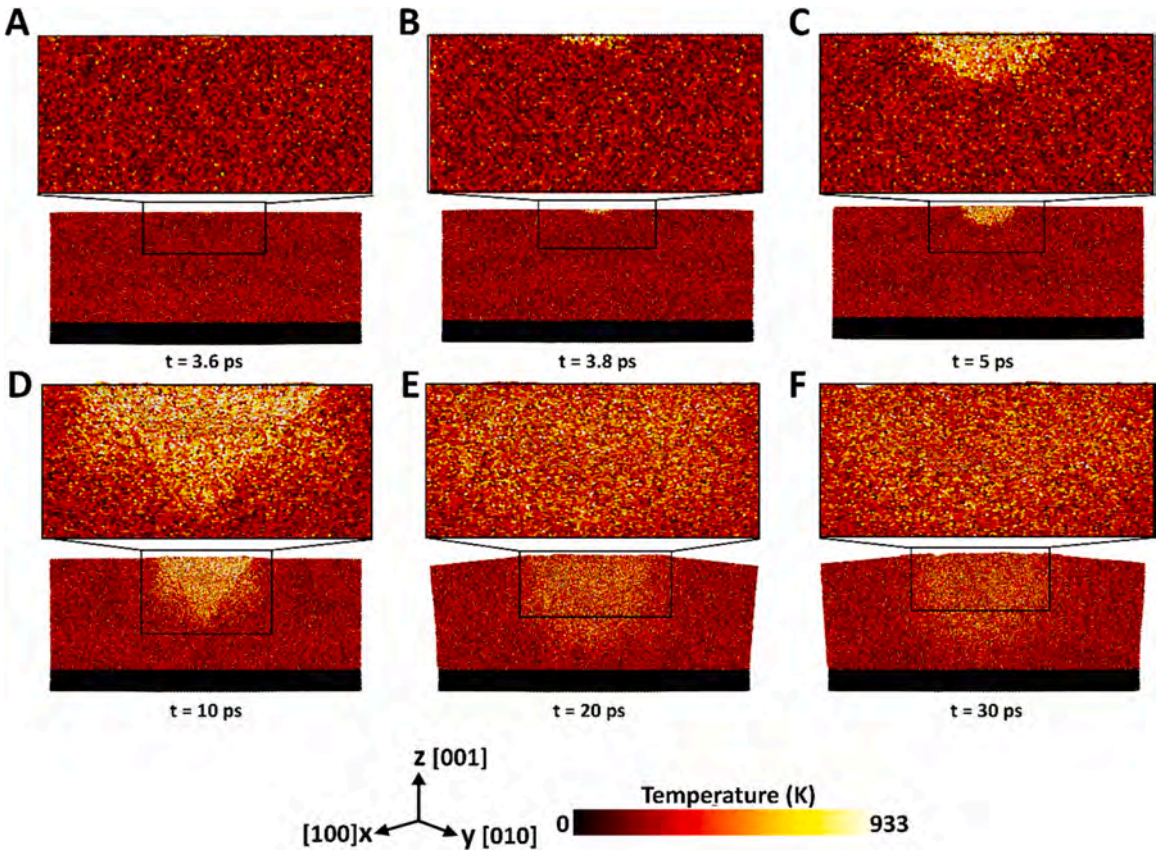

Fig. 3. Temperature distribution of the Fe particle-Al substrate model at the onset of impact at an impact velocity of 1200 m/s. A just before impact, B onset of particle–substrate contact, C and D formation and extension of melted interface, E and F solidification process.

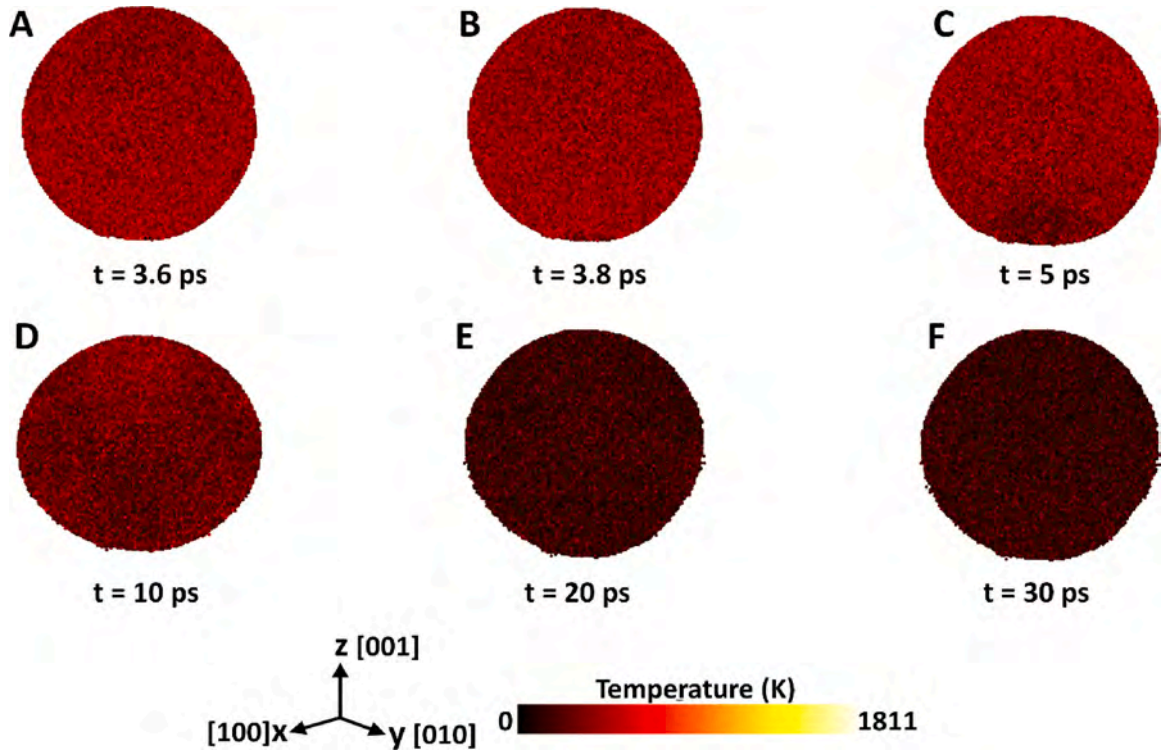

Fig. 4. Evolution of the temperature distribution within the modeled Fe particle during the simulation at selected time intervals.

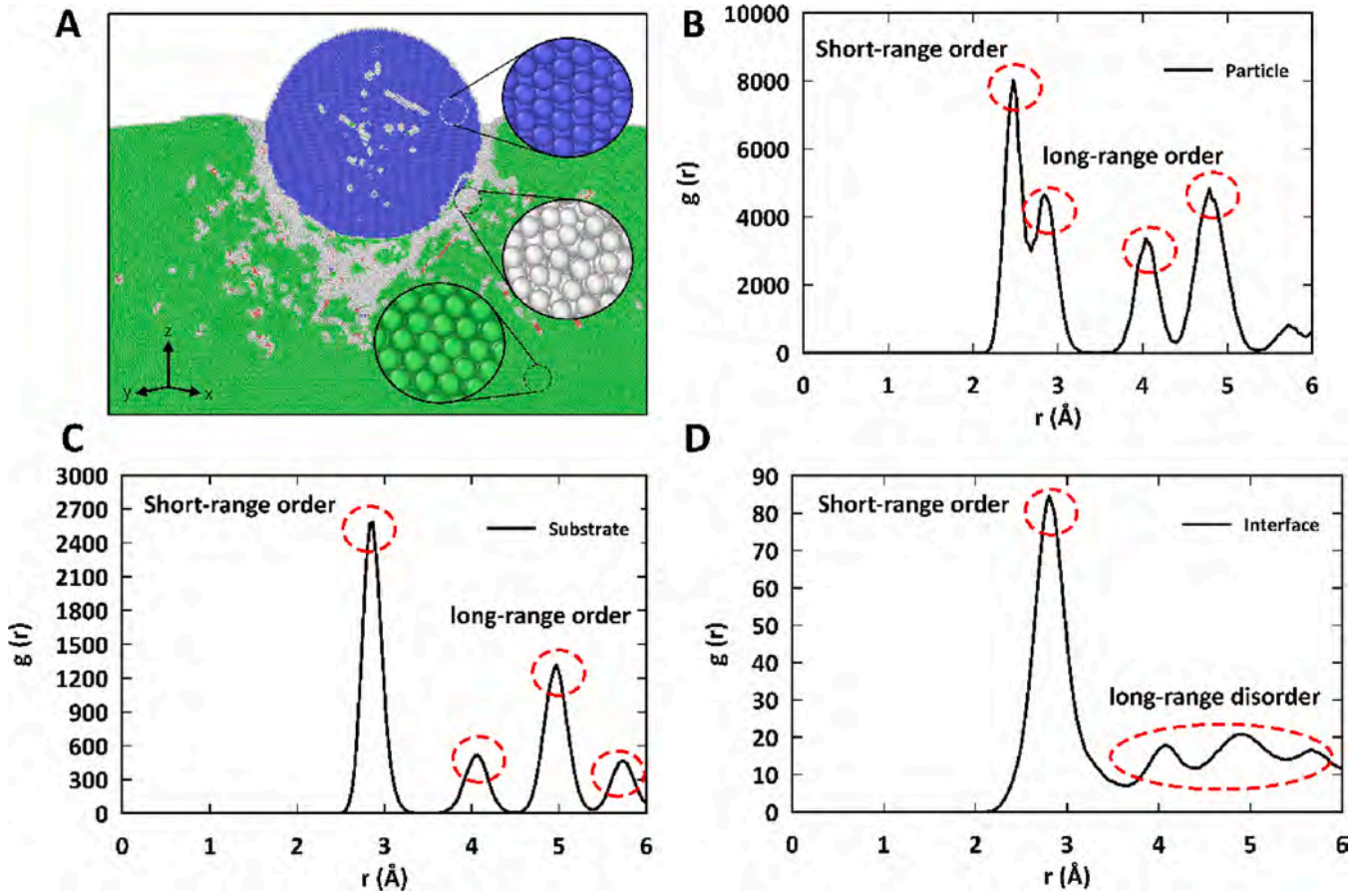

Fig. 5. Atomic configuration of the Fe particle/substrate system and corresponding RDFs for the particle, substrate, and interface regions. A shows different selected regions, B and C The particle and substrate exhibit pronounced short- and long-range crystalline order, whereas in D the interface retains short-range order with a significant reduction in long-range structural ordering, indicating the formation of a disordered interfacial region.

pronounced first peak corresponding to short-range atomic ordering, followed by several distinct peaks at larger interatomic distances, indicating the presence of long-range order and the preservation of crystalline structures. In contrast, the RDF of the interfacial region (Fig. 5d) shows only a prominent first peak at approximately 2.8 Å, while the subsequent peaks disappear and are replaced by broad, weak oscillations. The retention of short-range order together with the loss of long-range order is a characteristic feature of amorphous materials. Therefore, the RDF analysis clearly demonstrates that the interfacial region undergoes amorphization following impact and re-solidification. Since the formation of an amorphous structure under such conditions results from localized melting followed by rapid quenching, these findings are consistent with the occurrence of transient interfacial melting and, when considered together with the experimental observations, provide support to the proposed mechanism.

The MD simulations suggest the formation of a transient molten interfacial layer. To obtain further experimental evidence and evaluate its implications for IIS formation within the IAZ and for the segregation of Mg and O at the Fe particle–Al alloy interface, detailed site-specific electron microscopy analyses were performed. These mechanisms are better visualized through pairing electron microscopy and MD data as shown in Fig. 6. We now briefly explain how IIS might occur. At temperatures above the *solidus*, a two-phase region forms, *i.e.* the solid-liquid mushy surface layer (see Fig. 6A-B). It is important emphasizing that at the interface between the Fe particle and the Al alloy substrate, SAED pattern reveals the presence of Debye-Scherrer rings (see Fig. 6C), which corroborate the observed elemental segregation of O and Mg at this specific site (see Fig. 6D). As the solubility of the main alloying elements Si and Mg is significantly higher in the liquid phase than in the solid phase (partitioning coefficient $k = X_S/X_L$; $k_{Si} = 0.11$, $k_{Mg} = 0.51$) [56] these elements accumulate in the liquid phase, especially Si, for its around ten times higher solubility compared to the solid phase. Upon rapid cooling, which is the case here, due to the extreme temperature gradient, the mushy layer resolidifies under non-equilibrium, thus leading to the segregation pattern shown in Fig. 6A and quantified in Fig. 6D (note that the Si content in the initially liquid phase amounts to several at%; see Fig. 2D). With the higher partitioning coefficient, Mg is only moderately rejected from the solid into the liquid. However, Mg shows a high tendency to segregate to the surface of Al alloys mainly due to its lower surface energy and higher affinity for oxidation [57], which results in the formation of an Mg-rich oxide at the interface, as shown in Fig. 2F. Below the mushy zone, Mg and Si segregation lead to the formation of Mg, Si-rich precipitates as shown in Fig. 2F (precursor of ß-phase, Mg_2Si [58]), which contribute to hardening in this site-specific dependency, promoting Fe particle-substrate bonding upon solidification and cooling.

It should be pointed out that the formation of Mg-Si precipitates is a diffusion-controlled kinetic process that, in addition to elevated temperatures, requires a sufficient temperature–time window for atomic diffusion, segregation, and clustering of Mg and Si atoms. Although severe plastic deformation can induce localized temperature rises, such thermal excursions are typically short-lived and may not provide adequate conditions for the nucleation and growth of Mg-Si precipitates. In contrast, localized melting can prolong the local thermal cycle through the release of latent heat during re-solidification, thereby creating more favorable kinetic conditions for the diffusion, segregation, and precipitation of Mg and Si. Furthermore, although solid-state heating may promote elemental segregation or phase separation, it would not normally be expected to produce the directional (non-equiaxed) segregation morphology observed in the present STEM analysis. Such a morphology is more commonly associated with rapid solidification from a transient liquid phase and is therefore consistent with the occurrence of localized transient melting at the particle-substrate interface.

The MD simulation results further support the possibility of transient interfacial melting. For an Al substrate impacted by an Fe particle at a

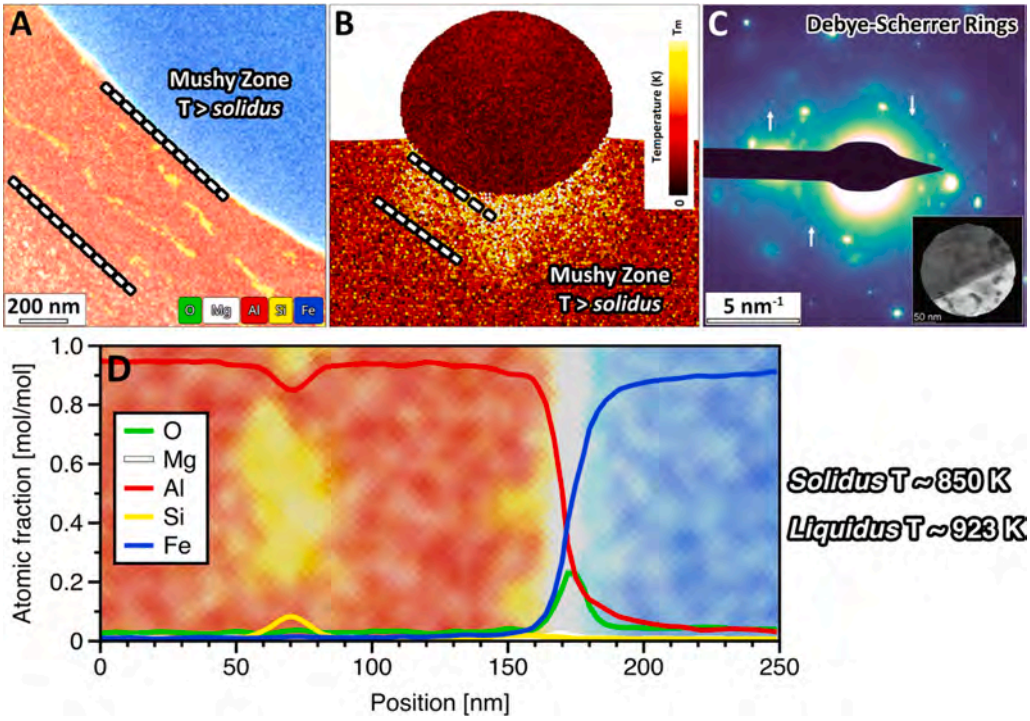

Fig. 6. A mushy zone is observed within the IAZ through STEM-EDX elemental mapping, as shown in the composition of the O, Mg, Al, Si and Fe elemental maps in A, suggesting that the local temperature has raised to slightly above the *solidus* temperature for this alloy system and has led to a clearly discernible separation of the main alloy elements (see Fig. 2D). In B, MD simulations suggest that the temperature of the mushy zone is above the *solidus*; the melting temperatures (Tm) of Al and Fe are 933 K and 1811 K, respectively. When taken along the interface, the SAED pattern in C reveals Debye-Scherrer Rings consistent with both observations of IIS. The local chemistry profile in D indicates pronounced segregation of Si and an interface rich in O and slightly rich in Mg.

velocity of 1200 m/s, at a simulation time of 10 ps, when a relatively coherent interface has formed between the particle and the substrate, approximately 31.71% of the interfacial atoms reach temperatures of 660 °C or higher, while an additional 27.98% fall within the temperature range of 560–660 °C (See Fig. 9b). Consequently, nearly 60% of the interfacial atoms are either within or very close to their melting regime, consistent with the Al–Si phase diagram [72]. (See Fig. S5). These results indicate that the conditions necessary for transient localized melting at the interface were achieved. The subsequent release of latent heat during re-solidification can extend the thermal dwell time and facilitate the diffusion and segregation processes required for Mg-Si precipitate formation.

During temperature dissipation in the post-melting stage, another distinctive feature of the IAZ is its extremely small subgrain size of ≈ 100 nm, which corresponds approximately to the distance between the Si segregation bands. Two events may be responsible for this

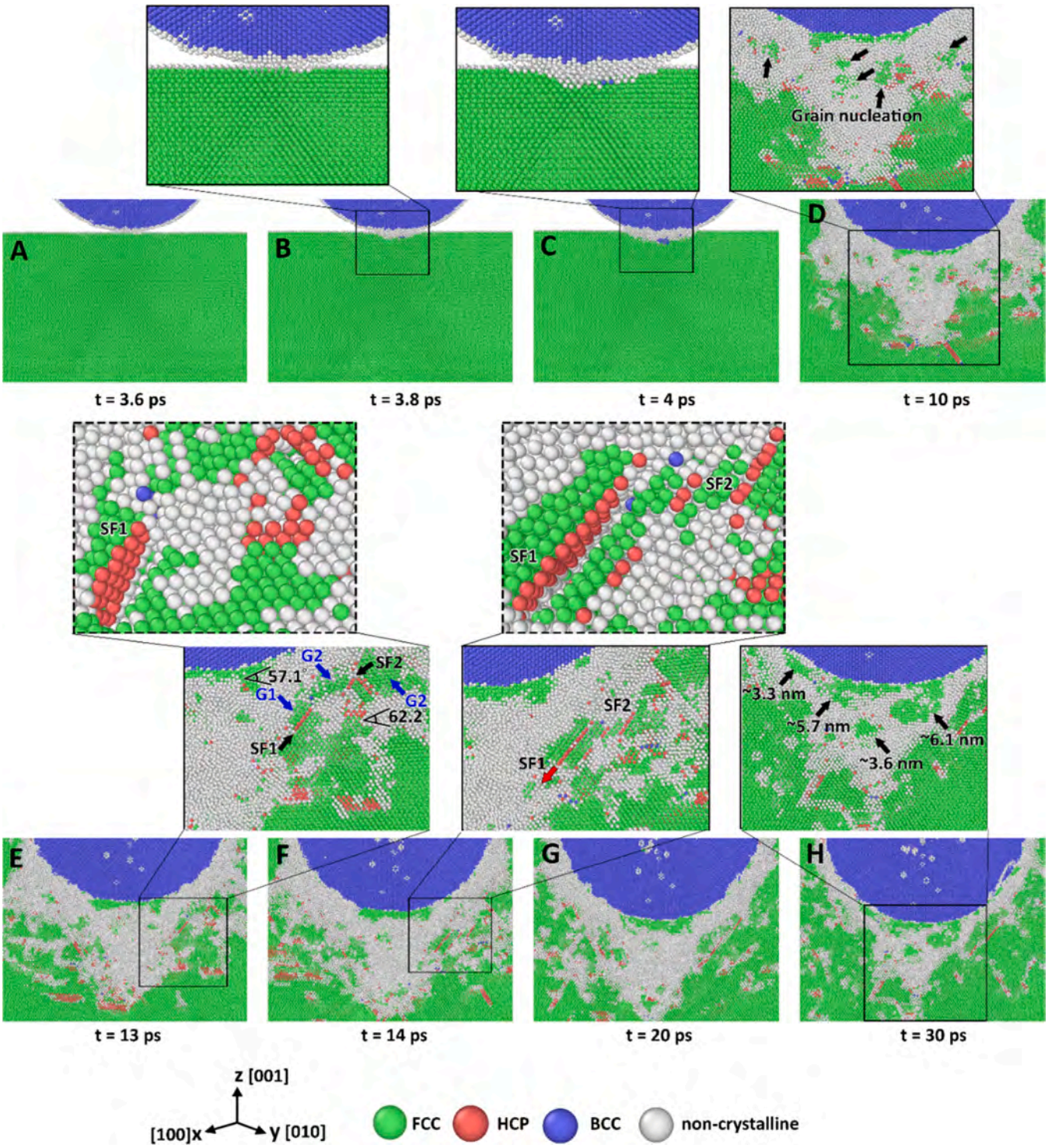

Fig. 7. Microstructural changes during the impact of Fe particle on the Al substrate at an impact velocity of 1200 m/s based on the PTM analysis. A-C formation of the mushy interface, D initiation of the grain nucleation process, E formation of SF planes within the grains with high degree of misorientation, F expansion of SFs accompanied by grain growth, G grain coarsening, H average size of the new grains.

observation. On one hand, the very high cooling rates yield extremely high nucleation rates and suppress grain growth. On the other hand, after complete solidification of the liquid IAZ fraction, the huge thermal gradient poses strong compressive/tensile stresses in the shallow IAZ layer producing a high dislocation density [59], which in turn promotes the formation of a very fine grain structure through dynamic recrystallisation or recovery. Moreover, geometrically induced dislocations, formed during the cooling process, arise due to the thermal mismatch between the Fe particle and the Al alloy substrate. This mismatch is a result of the differing coefficients of thermal expansion between the Al AA6082-T4 alloy ($\approx 24{\cdot}10^{-6}$ K^{-1}) and Fe ($\approx 12{\cdot}10^{-6}$ K^{-1}). Such geometrically induced dislocations may exert a similar effect [60].

Thermal stresses induced by the temperature gradient during IAZ cooling, including tensile stresses on the surface and compressive stresses in the substrate, lead to geometric distortions. This phenomenon plausibly explains the observed particle-substrate detachment at the central impact area, while metallurgical bonding is evident on the lateral sides of the Fe particle (see Figs. 1B and 1E). The metallurgical bond is characterized by the formation of a continuous Fe-Al interface without any discernible interfacial gap. Moreover, the distinct contrast observed within the interfacial layer in STEM images suggests elemental intermixing across the interface, further confirming the development of a metallurgically bonded region. Another potentially contributing factor to the formation of this detached area might be the increased heating observed in the central region of the impact zone, as illustrated in Fig. 3D. This localized rise in temperature and subsequent mushy zone formation can result in enhanced solidification shrinkage, potentially leading to the detachment phenomenon observed in the south pole region. The formation of Mg, Si-rich precipitates observed within the microstructure, especially in trans-granular positions at greater depths beneath the IAZ, as illustrated in the Fig. 2E, can be explained by the thermal effect of residual heat during cooling, whereby the latent heat of the liquid phase fraction may also play a key role. The main hardening phases present in AA6082 in the T4 state are GP (Guinier-Preston) zones, which can only be detected via high-resolution STEM [61]. The rounded precipitates observed below the IAZ are much bigger than the characteristic GP zones of the substrate in T4 state, suggesting that in this region, the precipitates are hardening phases approaching thermodynamic equilibrium.

The microstructural effects described above reflect the post-impact state. Structural events at the atomic scale that give rise to defect formations, as revealed by MD simulations, are no longer observable via electron microscopy as they have been annealed out through the acting thermal mechanisms. To investigate the underlying physics of the re-solidification/recrystallization/recovery phenomenon occurring in the IAZ, we systematically monitored the microstructural evolution within this region at different stages of particle impact within the MD simulations. Accordingly, Fig. 7 tracks dynamic recovery in the IAZ region from the initial moment of the impact to the final step of deposition by means of the Polyhedral Template Matching (PTM). As depicted in Fig. 7A-C, during the initial instants of impact, the primary interface at the contact surface between the particle and the substrate forms a mushy microstructure. At 10 ps, the initial formation of grain embryos occurs within the melted interface region (See Fig. 3D). As the cooling persists over time, these grains continue to grow, ultimately forming GBs. According to a study by Reddy et al. [26], these new grains are locked within GBs and thus experience considerable shear stress transfer caused by particle penetration to the substrate through the GBs. Figure S6 presents the atomic shear strain distribution at the initial stage of impact. A significant transfer of shear stress from the particle to the substrate is observed, which plays a crucial role in the formation of grains that exhibit high residual shear strain during the re-solidification stage of the mushy IAZ and severe plastic deformation caused by impact as detailed in [62,63]. One possible mechanism to reduce shear strain within grains is the formation of stacking fault (SF) planes during the recovery stage [64–66], as clearly observed at 13 ps and 14 ps time intervals (See SF1 and SF2 in Fig. 7e & f).

Fig. 7e shows the misorientation degree of GBs calculated for G1/G2 and G2/G3 grains. The HCP lamellae are formed from GBs with the highest misorientation degree relative to the neighboring grain. As a result, grains with these HCP lamellae can be referred to as shear grains, distinguishing them from other grain types. As shown in Fig. 7F, the shear grain G1 grows in the direction indicated by the red arrow, and the SFs also expand along the same direction. Moreover, the grains continue to grow, and the SFs extend at the 20 ps time step, as illustrated in Fig. 7G. Most of the grains formed during this phase contain high-angle GBs. Such boundaries are characteristic of recrystallization and recovery processes induced by intense deformation or rapid non-equilibrium cooling in the mushy IAZ [67–69]. These high-angle GBs play a crucial role for two primary reasons. First, their significant atomic disordering and elevated energy facilitate the diffusion of substitutional alloying elements, promoting precipitate formation, as discussed earlier. Second, these boundaries act as barriers to dislocation motion between grains. As a result, they contribute to increased mechanical strength in the vicinity of the interface.

Fig. 7h shows grain size distribution in the final microstructure of the system, displaying the presence of ultrafine grains, indicating significant shear strain localized within the IAZ. These findings demonstrate that the majority of the ultrafine grains produced formed during the dynamic recovery do not contain HCP lamellas once solidification is complete. This observation substantiates the absence of such crystalline defects, a conclusion further corroborated by TEM analysis.

Subgrain formation, which is directly influenced by the melting phenomenon and thermal recovery, is likely to be significantly affected by the impact velocity, as it can be assumed that this determines the extent of the formation of the liquid fraction. To shed more light on this issue, Fig. 8A-F demonstrate the resulting microstructures of the system following impacts of various velocities in MD simulations. The results indicate that increasing impact velocity leads to the formation of greater number of grains with reduced average grain size, thereby showing a direct correlation between impact energy and the recrystallization/recovery phenomena. Fig. 9A provides quantitative evidence for this trend, showing that as the impact velocity increases from 700 to 1200 m/s, the average grain size in the substrate drops from 6.0 $\pm$ 0.6–4.9 $\pm$ 0.6 nm, representing a reduction of about 22%.

Fig. 9B shows that as the impact velocity rises, a much larger portion of atoms enter melted and pre-melted states. This can be attributed to a larger melt volume/area formed at higher impact velocities, providing favorable conditions for the nucleation of a larger fraction of grains, thus in line with the smaller grain sizes inherent to higher impact velocities. Thus, the average grain size in the final IAZ is smaller at higher impact velocities. These findings are in agreement with the experimental work of Dowding & Schuh [70], who demonstrated that in regimes of extreme rate plastic deformation, increasing the interface temperature through higher impact velocity led to improved metallurgical bonding and enhanced hardness.

Another important point to note is that, as illustrated in Fig. 9B, the temperature in the interfacial region consistently reaches the melting point at all the studied velocities. This consistent melting at the interface facilitates bonding between the particle and substrate, as recently described [71]. The resulting liquid-like interface indicates that the generation of a liquid fraction is an important driving force behind recrystallization and recovery.

The results discussed in this study indicate that, in certain dissimilar cold spray systems exhibiting significant differences in mechanical properties, crystal structure, and deformability between the particle and the substrate, the transient formation of a nanoscale molten interfacial layer may facilitate and accelerate the establishment of metallurgical bonding. However, this transient melting is not proposed as a prerequisite for bonding, since metallurgical bonding can also be achieved through well-established solid-state mechanisms. Owing to the confinement of this phenomenon to a nanoscale region and its rapid re-

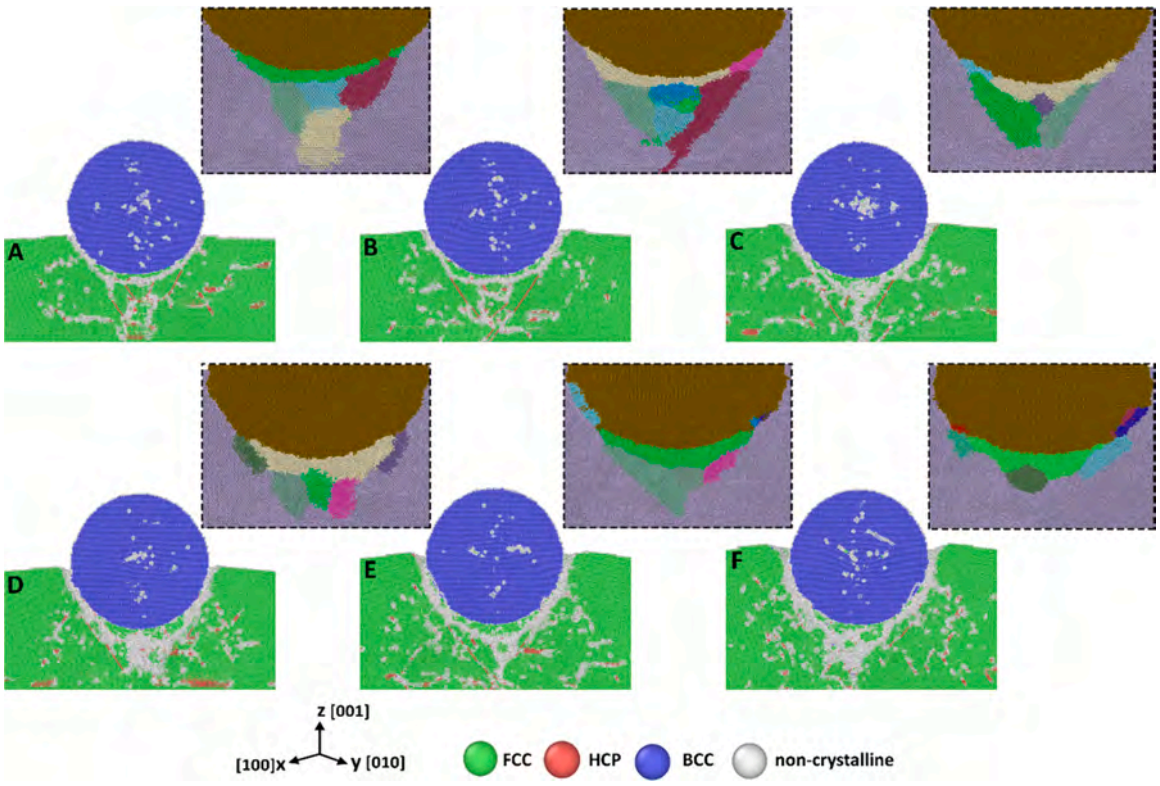

Fig. 8. Microstructural evolution during the impact of Fe particle on the Al substrate at different impact velocities based on PTM and grain segmentation analyses. A 700 m/s, B 800 m/s, C 900 m/s, D 1000 m/s, E 1100 m/s, F 1200 m/s.

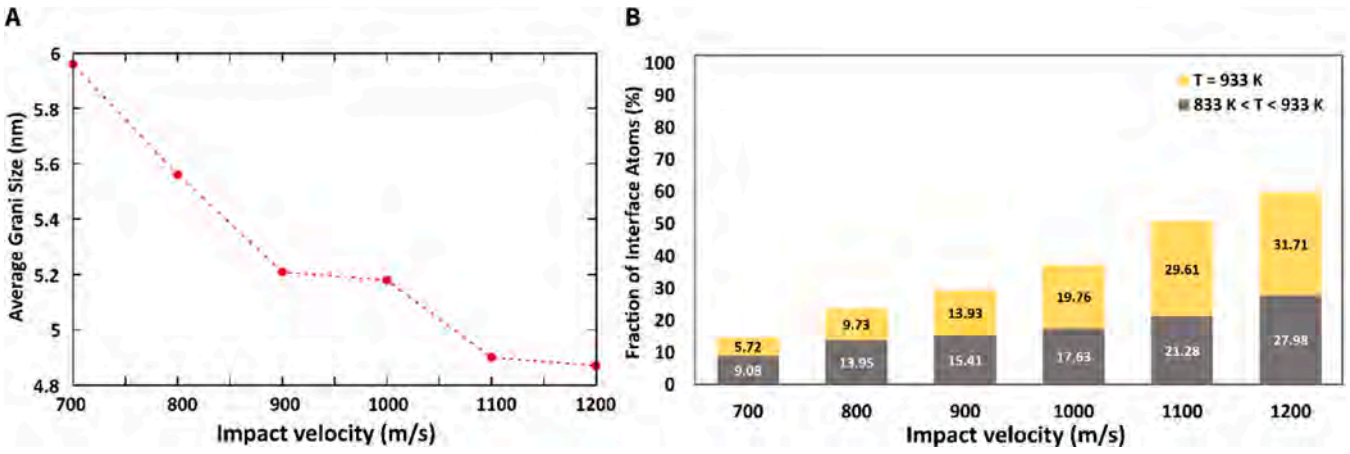

Fig. 9. Microstructural characterization of the Al substrate upon Fe particle impact at various velocities. A average grain size in the IAZ; B interfacial temperature distribution.

solidification under the extremely high cooling rates associated with particle impact, neither the particle nor the substrate undergoes bulk melting. Therefore, the overall nature of the cold spray process remains that of a solid-state process.

4. Conclusions

Metallurgical bonding resulting from high-velocity particle impact is considered to be primarily controlled by severe plastic deformation, leading to significant microstructural alterations and native oxide layer rupture, which promote metallurgical bonding at the particle–substrate interface. Based on the recent literature, dynamic recrystallization facilitated by deformation twinning can occur at exceptionally high velocities, yielding ultrafine-grained structures that strengthen interfacial bonding. Yet, most mechanistic-thermomechanical theories, including those involving critical particle velocity and ASI, which are fundamentally rooted in plasticity-related descriptions, mainly apply to materials with similar properties and do not account for the role of interfacial phase transitions. When dealing with dissimilar systems, our study indicated that additional interfacial phenomena contribute to metallurgical bonding beyond these established mechanisms at the atomic scale. Here, pairing advanced microscopic examinations and MD simulations, we reveal localized interfacial melting and subsequent rapid re-solidification as fundamental mechanisms for achieving robust metallurgical bonding between a hard Fe particle and a soft AA6082-T4 alloy substrate during solid-state CS deposition. An oxygen-rich interfacial layer, approximately twice as thick as the native oxide, was also observed at the interface; together with the experimentally observed Si

and Mg segregation, the formation of Mg-Si-rich precipitates, the interfacial microstructural features, and the MD simulation results, this observation is consistent with the occurrence of transient melting. Several transformative changes occur in the interfacial region and the IAZ as a result of these events: (i) the intense transfer of impact energy and ensuing localized melting at the interface and in the IAZ drive pronounced Si segregations and the emergence of Mg- and Si-rich precipitates, which are entirely absent in the substrate's original T4 state; (ii) in addition to severe plastic deformation, localized melting at the interface is instrumental in the formation of ultrafine grains within the IAZ, attributed to an increased nucleation rate resulting from the extremely high cooling rate in this region and to efficient recovery mechanisms that repair lattice defects caused during rapid cooling. Together, these changes underscore a dynamic interplay of thermal and mechanical forces that fundamentally reshape the microstructure and properties of the IAZ in dissimilar systems. The proposed mechanism is supported by the combined interpretation of the experimental observations and atomistic insights provided by MD simulations. While the simulations are intended to explain the fundamental interfacial processes rather than quantitatively reproduce the experimental CS process, they provide valuable mechanistic insight into phenomena that are difficult to access experimentally. We anticipate that these insights on melting and its subsequent microstructural transitions are key to improving interfacial bonding strength between powder particles and substrates of mismatched mechanical properties. This knowledge is crucial for advancement of multi-material solid state welding and next generation additive manufacturing.

CRediT authorship contribution statement

Arash Kardani: Writing – original draft, Visualization, Validation, Software, Methodology, Investigation. **Matheus A. Tunes:** Writing – original draft, Visualization, Methodology, Investigation, Funding acquisition. **Peter J. Uggowitzer:** Writing – review & editing, Visualization, Supervision, Methodology. **Hamid Assadi:** Writing – review & editing, Conceptualization. **Sara Bagherifard:** Writing – review & editing, Supervision, Methodology, Funding acquisition, Conceptualization.

Declaration of Competing Interest

The authors declare that they have no known competing financial interests or personal relationships that could have appeared to influence the work reported in this paper.

Acknowledgments

The authors acknowledge Mr. Kiran Tulasagiri Raddi for the preparation of the cold spray sample. AK and SB acknowledge funding from the European Research Council (ERC) under the European Union's Horizon 2021 research and innovation programme (ArcHIDep ERC-Co project, grant agreement n. 101044228). Views and opinions expressed are, however, those of the authors only and do not necessarily reflect those of the European Union or the European Research Council Executive Agency. Neither the European Union nor the granting authority can be held responsible for them. MAT, PJU acknowledge funding from Austrian Research Promotion Agency (FFG) within the project 3DnanoAnalytics (FFG-No 858040).

Appendix A. Supporting information

Supplementary data associated with this article can be found in the online version at doi:10.1016/j.addma.2026.105338.

Data availability

Data will be made available on request.

References

[1] D. Gu, X. Shi, R. Poprawe, D.L. Bourell, R. Setchi, J. Zhu, Material-structure-performance integrated laser-metal additive manufacturing, Science 372 (6545) (2021) eabg1487.
[2] Z. Su, L. Yin, H. Jiang, L. Zhang, Y. Chen, L. Zhang, H. Zhang, W. Feng, Research progress of electromagnetic pulse welding technology: a review, J. Mater. Res. Technol. 36 (2025) 217–235.
[3] H. Liu, W. Fan, Z. Xu, C. Sun, Y. Wu, J. Ju, J. Ma, Research progress of solid-phase welding technology between magnesium and dissimilar metals, J. Mater. Res. Technol. 38 (2025) 5409–5440.
[4] E.M. Bringa, K. Rosolankova, R.E. Rudd, B.A. Remington, J.S. Wark, M. Duchaineau, D.H. Kalantar, J. Hawreliak, J. Belak, Shock deformation of face-centred-cubic metals on subnanosecond timescales, Nat. Mater. 5 (10) (2006) 805–809.
[5] A. Heydari Astaraee, S. Bagherifard, Structural Integrity of Metal Deposits Obtained Using Cold Spray Solid-State Deposition, in, in: M.H.F. Aliabadi, W. O. Soboyejo (Eds.), Comprehensive Structural Integrity (Second Edition), Elsevier, Oxford, 2023, pp. 786–809.
[6] R.H.A. Shiddiegy, A. Wikarta, A.S. Pramono, Suwarno, J.-T. Yohanes, Tsai, Addressing challenges in deposition efficiency and material compatibility in low-pressure cold spray systems, Results Eng. 26 (2025) 105065.
[7] S. Bagherifard, J. Kondas, S. Monti, J. Cizek, F. Perego, O. Kovarik, F. Lukac, F. Gaertner, M. Guagliano, Tailoring cold spray additive manufacturing of steel 316 L for static and cyclic load-bearing applications, Mater. & Des. 203 (2021) 109575.
[8] Y. Zou, Cold spray additive manufacturing: microstructure evolution and bonding features, Acc. Mater. Res. 2 (11) (2021) 1071–1081.
[9] T. Schmidt, F. Gärtner, H. Assadi, H. Kreye, Development of a generalized parameter window for cold spray deposition, Acta Mater. 54 (3) (2006) 729–742.
[10] M.A. Adaan-Nyiak, A.A. Tiamiyu, Recent advances on bonding mechanism in cold spray process: a review of single-particle impact methods, J. Mater. Res. 38 (1) (2023) 69–95.
[11] R. Falco, S. Bagherifard, Cold spray additive manufacturing: a review of shape control challenges and solutions, J. Therm. Spray. Technol. 34 (4) (2025) 1023–1041.
[12] T.J. Lucas, C.A. Schuh, A single particle impact study on the effects of substrate strength and ductility on adhesion in cold spray, Int. J. Mech. Sci. 303 (2025) 110676.
[13] H. Assadi, H. Kreye, F. Gärtner, T. Klassen, Cold spraying – a materials perspective, Acta Mater. 116 (2016) 382–407.
[14] A.A. Tiamiyu, Y. Sun, K.A. Nelson, C.A. Schuh, Site-specific study of jetting, bonding, and local deformation during high-velocity metallic microparticle impact, Acta Mater. 202 (2021) 159–169.
[15] R. Nikbakht, S.H. Seyedein, S. Kheirandish, H. Assadi, B. Jodoin, Asymmetrical bonding in cold spraying of dissimilar materials, Appl. Surf. Sci. 444 (2018) 621–632.
[16] A.A. Tiamiyu, X. Chen, E.L. Pang, Y. Sun, J. Lienhard, J.M. LeBeau, K.A. Nelson, C. A. Schuh, Oxide layer delamination: an energy dissipation mechanism during high-velocity microparticle impacts, Appl. Surf. Sci. 574 (2022) 151673.
[17] A.A. Hemeda, C. Zhang, X.Y. Hu, D. Fukuda, D. Cote, I.M. Nault, A. Nardi, V. K. Champagne, Y. Ma, J.W. Palko, Particle-based simulation of cold spray: influence of oxide layer on impact process, Addit. Manuf. 37 (2021) 101517.
[18] G. Prashar, H. Vasudev, A comprehensive review on the analysis of adhesion strength of cold spray deposits, Results Surf. Interfaces 16 (2024) 100263.
[19] H. Assadi, F. Gärtner, T. Stoltenhoff, H. Kreye, Bonding mechanism in cold gas spraying, Acta Mater. 51 (15) (2003) 4379–4394.
[20] D. Guo, M. Kazasidis, A. Hawkins, N. Fan, Z. Leclerc, D. MacDonald, A. Nastic, R. Nikbakht, R. Ortiz-Fernandez, S. Rahmati, M. Razavipour, P. Richer, S. Yin, R. Lupoi, B. Jodoin, Cold spray: over 30 years of development toward a hot future, J. Therm. Spray. Technol. 31 (4) (2022) 866–907.
[21] C.-J. Li, W.-Y. Li, Y.-Y. Wang, Formation of metastable phases in cold-sprayed soft metallic deposit, Surf. Coat. Technol. 198 (1) (2005) 469–473.
[22] W.-Y. Li, C. Zhang, X. Guo, J. Xu, C.-J. Li, H. Liao, C. Coddet, K.A. Khor, Ti and Ti-6Al-4V coatings by cold spraying and microstructure modification by heat treatment, Adv. Eng. Mater. 9 (5) (2007) 418–423.
[23] G. Bae, Y. Xiong, S. Kumar, K. Kang, C. Lee, General aspects of interface bonding in kinetic sprayed coatings, Acta Mater. 56 (17) (2008) 4858–4868.
[24] T.J. Lucas, N.R. Barton, A.M. Saunders, C.A. Schuh, Modeling of melting and erosion in high velocity microparticle impacts, Acta Mater. (2025) 121488.
[25] S. Suresh, S.-W. Lee, M. Aindow, H.D. Brody, V.K. Champagne, A.M. Dongare, Mesoscale modeling of jet initiation behavior and microstructural evolution during cold spray single particle impact, Acta Mater. 182 (2020) 197–206.
[26] C.D. Reddy, Z.-Q. Zhang, S. Msolli, J. Guo, N. Sridhar, Impact induced metallurgical and mechanical interlocking in metals, Comput. Mater. Sci. 192 (2021) 110363.
[27] Y. Xiong, K. Kang, G. Bae, S. Yoon, C. Lee, Dynamic amorphization and recrystallization of metals in kinetic spray process, Appl. Phys. Lett. 92 (19) (2008).

[28] R. Thevamaran, O. Lawal, S. Yazdi, S.-J. Jeon, J.-H. Lee, E.L. Thomas, Dynamic creation and evolution of gradient nanostructure in single-crystal metallic microcubes, Science 354 (6310) (2016) 312–316.
[29] J. Schneider, R. Radzilowski, Welding of very dissimilar materials (Fe-Al), JOM 66 (10) (2014) 2123–2129.
[30] L.-L. Li, Y. Su, I.J. Beyerlein, W.-Z. Han, Achieving room-temperature brittle-to-ductile transition in ultrafine layered Fe-Al alloys, Sci. Adv. 6 (39) (2020) eabb6658.
[31] R. Beygi, I. Galvão, A. Akhavan-Safar, H. Pouraliakbar, V. Fallah, L.F.M. da Silva, Effect of alloying elements on intermetallic formation during friction stir welding of dissimilar, Met. A Crit. Rev. Alum. /Steel Met. 13 (4) (2023) 768.
[32] J.A. Sørhaug, H.L. Korsvold, A. Celotto, Ø. Grong, P.E. Vullum, R. Holmestad, Precipitate stability in the heat-affected zone of a welded Al–Mg–Si–Cu alloy, J. Mater. Res. Technol. 42 (2026) 11712–11722.
[33] L.A. Giannuzzi, F.A. Stevie, A review of focused ion beam milling techniques for TEM specimen preparation, Micron 30 (3) (1999) 197–204.
[34] J. Mayer, L.A. Giannuzzi, T. Kamino, J. Michael, TEM Sample Preparation and FIB-Induced Damage, MRS Bull. 32 (5) (2007) 400–407.
[35] P. Wu, A. Kardani, M. Liu, S. Bagherifard, Atomic-level insights into cold spray deposition of Cu-GNPs composite coatings, Surf. Coat. Technol. 516 (2025) 132763.
[36] L.M. Pereira, A. Zúñiga, B. Jodoin, R.G.A. Veiga, S. Rahmati, Unraveling jetting mechanisms in high-velocity impact of copper particles using molecular dynamics simulations, Addit. Manuf. 75 (2023) 103755.
[37] M.I. Mendelev, D.J. Srolovitz, G.J. Ackland, S. Han, Effect of Fe segregation on the migration of a non-symmetric $\sum$5 tilt grain boundary in Al, J. Mater. Res. 20 (1) (2005) 208–218.
[38] J. Syarif, K. Badawy, H.A. Hussien, Atomistic simulation of the diffusion behavior in Al-Fe, Nucl. Mater. Energy 29 (2021) 101073.
[39] Y. Zhang, T. Zhao, X. Yu, J. Huang, The Al-Fe Intermetallic Compounds and the Atomic Diffusion Behavior at the Interface of Aluminum-Steel Welded Joint, Metals 13 (2) (2023) 334.
[40] Z.El Chlouk, W. Kassem, M. Shehadeh, R.F. Hamade, On the mechanical response and intermetallic compound formation in Al/Fe interface: molecular dynamics analyses, Philos. Mag. 100 (24) (2020) 3041–3060.
[41] L. Yang, F. Zhang, C.-Z. Wang, K.-M. Ho, A. Travesset, Implementation of metal-friendly EAM/FS-type semi-empirical potentials in HOOMD-blue: A GPU-accelerated molecular dynamics software, J. Comput. Phys. 359 (2018) 352–360.
[42] A.P. Thompson, H.M. Aktulga, R. Berger, D.S. Bolintineanu, W.M. Brown, P. S. Crozier, P.J. in 't Veld, A. Kohlmeyer, S.G. Moore, T.D. Nguyen, R. Shan, M. J. Stevens, J. Tranchida, C. Trott, S.J. Plimpton, LAMMPS - a flexible simulation tool for particle-based materials modeling at the atomic, meso, and continuum scales, Comput. Phys. Commun. 271 (2022) 108171.
[43] P. Gao, C. Zhang, R. Wang, G. Deng, J. Li, L. Su, Tamping effect during additive manufacturing of copper coating by cold spray: a comprehensive molecular dynamics study, Addit. Manuf. 66 (2023) 103448.
[44] M. Parrinello, A. Rahman, Crystal structure and pair potentials: a molecular-dynamics study, Phys. Rev. Lett. 45 (14) (1980) 1196–1199.
[45] S. Rahmati, A. Zúñiga, B. Jodoin, R.G.A. Veiga, Deformation of copper particles upon impact: a molecular dynamics study of cold spray, Comput. Mater. Sci. 171 (2020) 109219.
[46] C.D. Reddy, Z.-Q. Zhang, S. Msolli, J. Guo, N. Sridhar, Impact velocity-dependent bonding mechanisms in metal cold spray, Surf. Coat. Technol. 433 (2022) 128085.
[47] H. Assadi, T. Schmidt, H. Richter, J.O. Kliemann, K. Binder, F. Gärtner, T. Klassen, H. Kreye, On parameter selection in cold spraying, J. Therm. Spray. Technol. 20 (6) (2011) 1161–1176.
[48] Y. Nikravesh, G. Frantziskonis, M.I. Latypov, K. Muralidharan, Atomistic characterization of impact bonding in cold spray deposition of copper, Materialia 28 (2023) 101736.
[49] I.Alabd Alhafez, O.R. Deluigi, N. Merkert, H.M. Urbassek, E.M. Bringa, Cluster impact into high-entropy alloys: deformation, hardness changes, and subgrain formation, J. Mater. Res. Technol. 42 (2026) 104–112.
[50] A. Stukowski, Visualization and analysis of atomistic simulation data with OVITO–the Open Visualization Tool, Model. Simul. Mater. Sci. Eng. 18 (1) (2010) 015012.
[51] P.M. Larsen, S. Schmidt, J. Schiøtz, Robust structural identification via polyhedral template matching, Model. Simul. Mater. Sci. Eng. 24 (5) (2016) 055007.
[52] J.F. Panzarino, T.J. Rupert, Tracking Microstructure of Crystalline Materials: A Post-Processing Algorithm for Atomistic Simulations, JOM 66 (3) (2014) 417–428.
[53] C.L. Kelchner, S.J. Plimpton, J.C. Hamilton, Dislocation nucleation and defect structure during surface indentation, Phys. Rev. B 58 (17) (1998) 11085–11088.
[54] J. Evertsson, F. Bertram, F. Zhang, L. Rullik, L.R. Merte, M. Shipilin, M. Soldemo, S. Ahmadi, N. Vinogradov, F. Carlà, J. Weissenrieder, M. Göthelid, J. Pan, A. Mikkelsen, J.O. Nilsson, E. Lundgren, The thickness of native oxides on aluminum alloys and single crystals, Appl. Surf. Sci. 349 (2015) 826–832.
[55] I. Polmear, D. StJohn, J.F. Nie, M. Qian, Light Alloys: Metallurgy of the Light Metals, Butterworth-Heinemann, 2017.
[56] M. Easton, D. StJohn, Grain refinement of aluminum alloys: Part I. the nucleant and solute paradigms-a review of the literature, Metall. Mater. Trans. A 30 (6) (1999) 1613–1623.
[57] C. Lea, C. Molinari, Magnesium diffusion, surface segregation and oxidation in Al-Mg alloys, J. Mater. Sci. 19 (7) (1984) 2336–2352.
[58] S. Pogatscher, H. Antrekowitsch, H. Leitner, T. Ebner, P.J. Uggowitzer, Mechanisms controlling the artificial aging of Al–Mg–Si Alloys, Acta Mater. 59 (9) (2011) 3352–3363.
[59] T. Matsuda, T. Sano, K. Arakawa, A. Hirose, Dislocation structure produced by an ultrashort shock pulse, J. Appl. Phys. 116 (18) (2014).
[60] N.A. Fleck, M.F. Ashby, J.W. Hutchinson, The role of geometrically necessary dislocations in giving material strengthening, Scr. Mater. 48 (2) (2003) 179–183.
[61] C. Li, C.D. Marioara, C. Hatzoglou, S.J. Andersen, R. Holmestad, Y. Li, Accelerating precipitation hardening by natural aging in a 6082 Al-Mg-Si alloy, Acta Mater. 281 (2024) 120396.
[62] S. Zhao, S. Yin, X. Liang, F. Cao, Q. Yu, R. Zhang, L. Dai, C.J. Ruestes, R.O. Ritchie, A.M. Minor, Deformation and failure of the CrCoNi medium-entropy alloy subjected to extreme shock loading, Sci. Adv. 9 (18) (2023) eadf8602.
[63] A.A. Tiamiyu, E.L. Pang, X. Chen, J.M. LeBeau, K.A. Nelson, C.A. Schuh, Nanotwinning-assisted dynamic recrystallization at high strains and strain rates, Nat. Mater. 21 (7) (2022) 786–794.
[64] D.F. Rojas, O.K. Orhan, M. Ponga, Dynamic recrystallization of Silver nanocubes during high-velocity impacts, Acta Mater. 212 (2021) 116892.
[65] A. Kardani, A. Montazeri, Metal-matrix nanocomposites under compressive loading: towards an understanding of how twinning formation can enhance their plastic deformation, Sci. Rep. 10 (1) (2020) 9745.
[66] Y. Tang, D.Y. Li, Dynamic response of high-entropy alloys to ballistic impact, Sci. Adv. 8 (32) (2022) eabp9096.
[67] D.A. Hughes, N. Hansen, High angle boundaries formed by grain subdivision mechanisms, Acta Mater. 45 (9) (1997) 3871–3886.
[68] A.M. Glezer, V.N. Varyukhin, A.A. Tomchuk, N.A. Maleeva, Nature of high-angle grain boundaries in metals subjected to severe plastic deformation, Dokl. Phys. 59 (8) (2014) 360–363.
[69] L.S. Tóth, B. Beausir, C.F. Gu, Y. Estrin, N. Scheerbaum, C.H.J. Davies, Effect of grain refinement by severe plastic deformation on the next-neighbor misorientation distribution, Acta Mater. 58 (20) (2010) 6706–6716.
[70] I. Dowding, C.A. Schuh, Metals strengthen with increasing temperature at extreme strain rates, Nature 630 (8015) (2024) 91–95.
[71] M.S. Khan, C.A. Schuh, Nanoscale interfacial melting enables bonding during high velocity microparticle impacts, Acta Mater. (2025) 121888.
[72] Q. Miao, D. Wu, D. Chai, Y. Zhan, G. Bi, F. Niu, G. Ma, Comparative study of microstructure evaluation and mechanical properties of 4043 aluminum alloy fabricated by wire-based additive manufacturing, Mater. & Des. 186 (2020) 108205.